AGU PUBLICATIONS

Space Weather

FEATURE ARTICLE
10.1002/2016SW001474

Key Points:
- Ionospheric weather monitored by total electron content (TEC)
- Dynamical development of ionospheric plasma bubbles (IPB)
- Influence of plasma bubbles on the GNSS-based positioning system

Correspondence to:
H. Takahashi,
hisao.takahashi@inpe.br

Citation:
Takahashi, H., et al. (2016), Ionospheric TEC Weather Map Over South America, *Space Weather*, *14*, 937–949, doi:10.1002/2016SW001474.

Received 19 JUL 2016
Accepted 7 OCT 2016
Accepted article online 8 OCT 2016
Published online 11 NOV 2016

Ionospheric TEC Weather Map Over South America

H. Takahashi[1], C. M. Wrasse[1], C. M. Denardini[1], M. B. Pádua[1], E. R. de Paula[1], S. M. A. Costa[2], Y. Otsuka[3], K. Shiokawa[3], J. F. Galera Monico[4], A. Ivo[1], and N. Sant'Anna[1]

[1]EMBRACE, Instituto Nacional de Pesquisas Espaciais, São José dos Campos, Brazil, [2]GRRP/CGED, Instituto Brasileiro de Geografia e Estatística, Rio de Janeiro, Brazil, [3]Institute for Space-Earth Environmental Research, Nagoya University, Nagoya, Japan, [4]Departamento de Cartografia, Universidade Estadual Paulista, Presidente Prudente, Brazil

Abstract Ionospheric weather maps using the total electron content (TEC) monitored by ground-based Global Navigation Satellite Systems (GNSS) receivers over South American continent, TECMAP, have been operationally produced by Instituto Nacional de Pesquisas Espaciais's Space Weather Study and Monitoring Program (*Estudo e Monitoramento Brasileiro de Clima Especial*) since 2013. In order to cover the whole continent, four GNSS receiver networks, (Rede Brasileiro de Monitoramento Contínuo) RBMC/Brazilian Institute for Geography and Statistics, Low-latitude Ionospheric Sensor Network, International GNSS Service, and Red Argentina de Monitoreo Satelital Continuo, in total ~140 sites, have been used. TECMAPs with a time resolution of 10 min are produced in 12 h time delay. Spatial resolution of the map is rather low, varying between 50 and 500 km depending on the density of the observation points. Large day-to-day variabilities of the equatorial ionization anomaly have been observed. Spatial gradient of TEC from the anomaly trough (total electron content unit, 1 TECU = 10^{16} el m^{-2} (TECU) <10) to the crest region (TECU > 80) causes a large ionospheric range delay in the GNSS positioning system. Ionospheric plasma bubbles, their seeding and development, could be monitored. This plasma density (spatial and temporal) variability causes not only the GNSS-based positioning error but also radio wave scintillations. Monitoring of these phenomena by TEC mapping becomes an important issue for space weather concern for high-technology positioning system and telecommunication.

Introduction

Earth's equatorial ionosphere presents dynamically temporal and spatial variations. During the day time, formation of the equatorial ionization anomaly (EIA) occurs due to the ionospheric fountain effect over the geomagnetic equator. After sunset a rapid uplifting of the *F* layer forms a postsunset equatorial ionization anomaly (PS-EIA) [*Kelley*, 2009]. In a certain condition the uplifting produces ionospheric irregularity (Rayleigh-Taylor instability) generating plasma bubbles along the geomagnetic field lines [*Kelley*, 2009]. The PS-EIA produces a large plasma density gradient from the trough region (over geomagnetic equator) to the crest region (10–15° geomagnetic north and south). Looking the gradient in terms of the total electron content (TEC unit of 1×10^{16}/m^{2}col), it varies from a few total electron content unit, 1 TECU = 10^{16} el m^{-2} (TECU) along the magnetic equator region to 20–50 TECU at the crest region depending on the day and season [*Bagiya et al*., 2009]. In the case of plasma bubbles, the TEC gradient is much steep, a difference of 30–50 TECU from the inside to outside of the bubble with a distance of hundreds of kilometers [*Takahashi et al*., 2015]. In addition to the spatial gradient of TEC, radio wave propagation inside of the plasma bubbles is affected by spatial irregularity of plasma density causing radio wave scintillations [*Kintner et al*., 2007].

The spatial and temporal variations of plasma density (and TEC) cause errors in Global Navigation Satellite Systems (GNSS)-based positioning services. A difference of 1 TECU, for example, may cause ~0.16 m of ionospheric range delay as presented in the next section. The demand of information on GNSS positioning error and radio wave quality has been increased significantly in the last decade, and today it becomes a crucial matter for operation of many kinds of space-based systems. Off-shore oil plant platform requires positioning accuracy of less than a few centimeters [*International Association of Oil & Gas Producers*, 2011]. High-technology agricultures also require a high positioning accuracy [*Stafford*, 2000]. Ground-based argumentation system for aircraft landing and takeoff also requires a high positioning accuracy and integrity of the information [*Federal Aviation Administration*, 2016]. For such high level of reliability for positioning systems, irregularity of ionospheric plasma contents is an important issue to monitor and overcome. Further to these applications, TEC monitoring has become a powerful tool for ionospheric study [*Nogueira et al*., 2015] and space weather [*Schrijver et al*., 2015].

Table 1. Procedure to Obtain VTEC From RINEX GPS Data

	Start
1	GPS data in RINEX format
2	Get: Time series of CODE: P_1 and P_2 (pseudorange in meters)
3	Get: Time series of phase values: L_1 and L_2 (wave numbers)
4	Cycle slip verification and correction
5	Calcul. Difference of pseudorange: $D_p = P_2 - P_1$ in meters
6	Calcul. Difference of L_1 and L_2: $D_L = (L_1/f_1 - L_2/f_2)*c$, where f_1 and f_2 are radio wave frequency (/s) and c: light velocity in m/s
7	Calcul. Ambiguity: $A(t) = D_L - D_p$ for each time series
8	Calcul. Averaged A value (A^*): using $>$ 1 h of time series of $A(t)$
9	Calcul. Slant TEC: STEC = 9.52($D_L - A^*$) − B_i
10	Calcul. Instrumental bias (B_i): for each receiver-satellite couple
11	Calcul. Slant factor: $S_i = \tau_1/\tau_0$, from the satellite zenith angle, θ, at the ionospheric height (navigation data)
12	Calcul. Vertical TEC: VTEC = STEC/S_i
	End

In order to attend such demands, Space Weather Study and Monitoring Program (*Estudo e Monitoramento Brasileiro de Clima Especial*, *EMBRACE)/Instituto Nacional de Pesquisas Espaciais* has been developing the ionospheric weather map based on TEC (TECMAP) and GPS signal scintillation map (S4) since 2013. TECMAPs over the South American continent with a 10 min time resolution are published on the EMBRACE internet website as a routine base [*Estudo e Monitoramento Brasileiro de Clima Especial* (*EMBRACE*) *site*, 2016]. The purpose of the present work is, first, to present the concept of TEC calculation using GNSS satellite radio waves. Typical TECMAPs for a normal condition, with plasma bubble activities and during the geomagnetic storm conditions, are presented. Then the ionospheric error range due to the TEC spatial gradient will also be discussed.

Observations

How to Calculate TEC

Phase and group delays of radio waves in the ionosphere are dependent on the total electron contents (TECs) along the ray path and the radio frequency, f (in hertz), with a simple relation [*Hoffmann-Wellenhof et al*., 1994]:

$$-d_p = d_g = 40.3[\mathrm{TEC}]/f^2 \ \text{ in } \ (\mathrm{m}) \tag{1}$$

where d_p and d_g represent, respectively, phase delay and group delay and [] indicates a physical content. One TEC unit measures 1×10^{16} el/m^{2}col, and it corresponds to approximately 0.16 m of the ionospheric delay.

Using a fact that the delay is a function of the frequency, one can also obtain TEC from a difference of delay between the two radio waves. GPS satellites, for example, transmit dual frequency radio wave signals from the orbit at an altitude of ~20,200 km: f_1: 1575.42 MHz and f_2:1227.60 MHz.

The signals are composed of binary phase-modulated carrier wave. Observables are the pseudorange (P) measured by using the code modulation and the accumulated carrier phase (L). Ground-based GPS receivers, therefore, observe both pseudorange (P_1 and P_2 in meters) and carrier wave phase (L_1 and L_2 in wave number). The difference of the pseudorange of P_1 and P_2 can provide TEC as [*Kantor et al*., 2000]:

$$[\mathrm{TEC}]_{p,i} = 9.52\left(P_{2,i} - P_{1,i}\right) - B_i \tag{2}$$

where i denotes the satellite PRN (Pseudo Ramdom Noise) number and B_i is an instrumental bias of satellite i and a ground receiver. It is a delay originated from the satellite transmitter and ground-based receiver hardware (response) systems. TEC is an integrated total electron content along the line of sight between the receiver and a GPS satellite (denoted as Slant TEC). It provides an absolute TEC value, but it is a coarse data (having a relatively large random error). On the other hand, the difference of the carrier

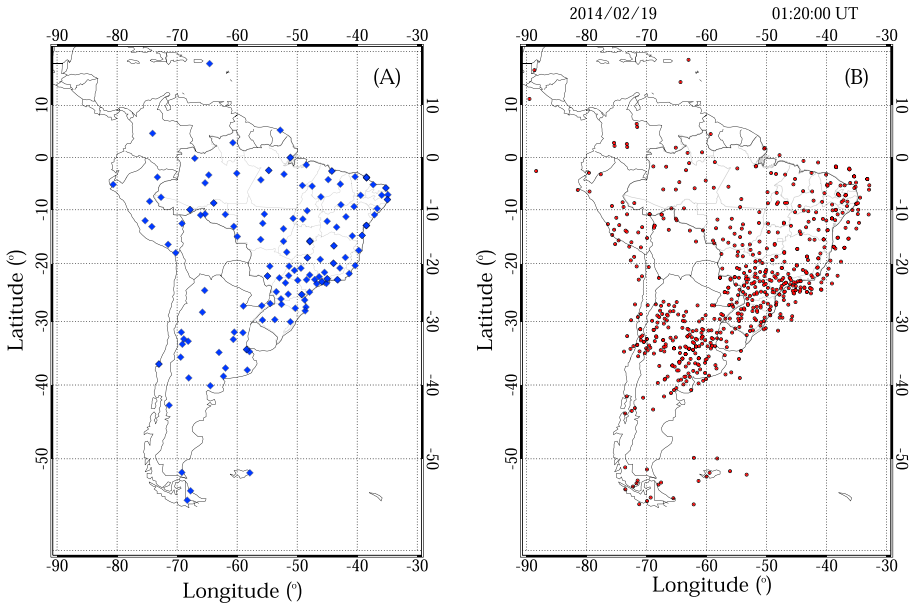

Figure 1. (a) Ground-based GNSS receiver sites by RBMC, IGS, LISN, and RAMSAC networks over South America. (b) An example of ionospheric pierce point distribution of the TEC measurement on the night of 19 February 2014.

phase between L_1 and L_2 is precise and less noisy, but it is a relative value having an ambiguity, not providing the absolute TEC value.

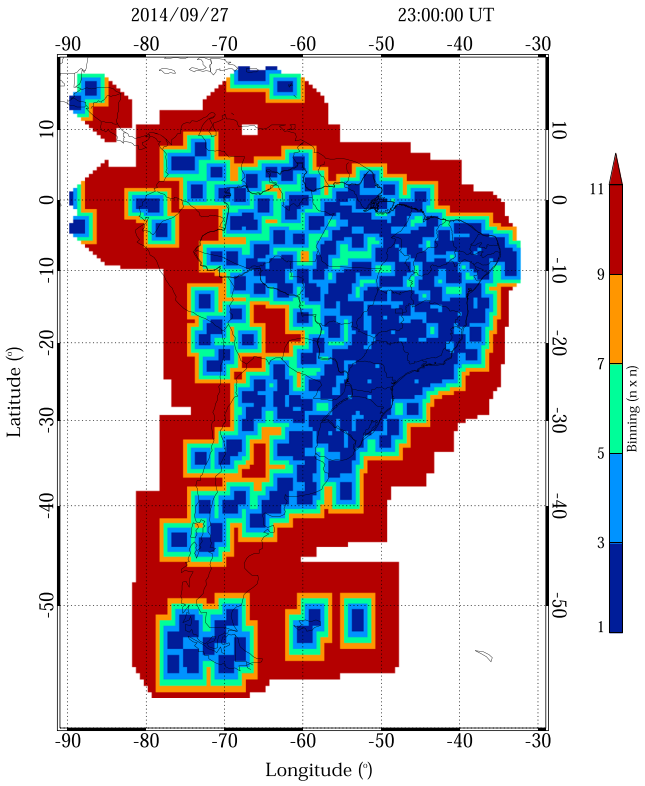

Figure 2. Spatial resolution map of TEC calculation on the night of 27 September 2014 at 23:00 UT; Blue: 3 × 3 element, light blue: 5 × 5 element, light green: 7 × 7, and brown: 9 × 9 elements. Each element has a 0.5° (~50 km) spatial extension.

The difference of the carrier phase between L_1 and L_2 is also related to TEC as

$$[\mathrm{TEC}]_{L,i} = 9.52\left(\Phi_{1,\ i} - \Phi_{2,i}\right) + A_i^* \quad (3)$$

where $\Phi = (L/f)^*c$ in meters, L is a wave number in the wave path, f is a frequency, and c is the velocity of light. A^* is a term of ambiguity originated from unknown absolute value of Φ_1 and Φ_2. It can be estimated by comparing (P_2-P_1) and (Φ_1-Φ_2) for each pair of satellite and receiver:

$$A_i^* = < \left(\Phi_{1,i} - \Phi_{2,i}\right) - \left(P_{2,i} - P_{1,i}\right) >$$

where $< >$ indicates time average during the satellite passage (normally 1–4 h). For the present work, we adopted 1 h averaging to fix the parameter A^*. In calculating A^* another ambiguity caused by carrier wave cycle splitting should be taken in account. The cycle slip can be found from the discontinuity of the carrier waves. The correction was carried out by using a same methodology developed by *Belwitt* [1990].

The instrumental bias (B_i), for each receiver and satellite, was obtained by comparing the uncalibrated TEC values from all of the satellite and receiver combinations using the least mean

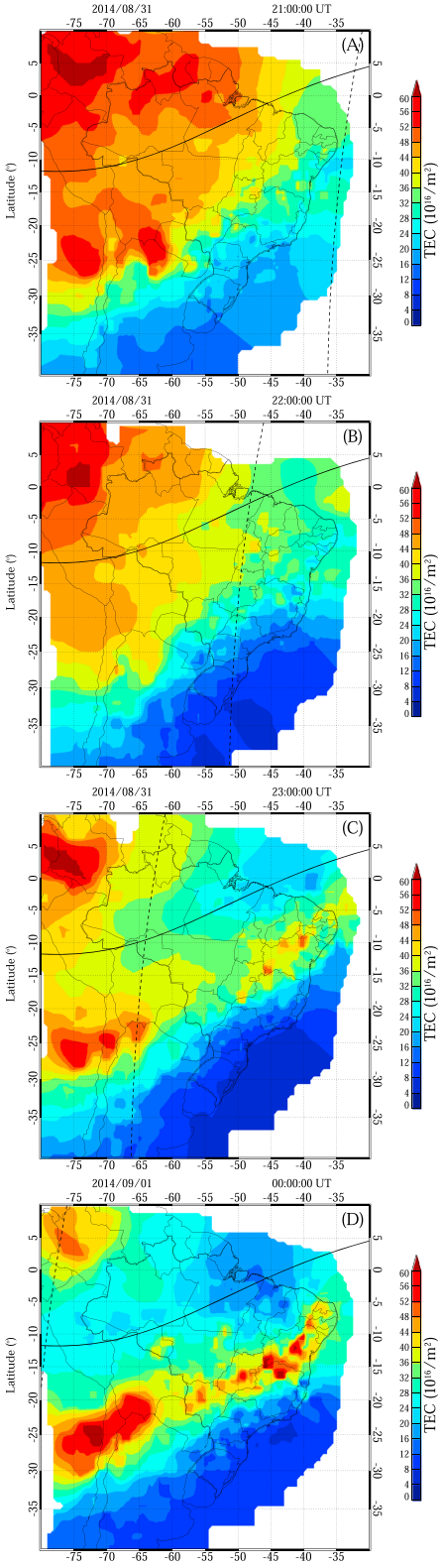

Figure 3. Color shaded TEC maps over South America on the evening of 31 August 2014, from (a) 21:00, (b) 22:00, (c) 23:00, and (d) 00:00 UT, showing development of the postsunset equatorial ionization anomaly. The black line indicates the geomagnetic equator, and the dashed line indicates solar terminator at around 300 km altitude.

square fitting method. We assumed that B_i would be constant during 24 h. The procedure of calculus was similar to those presented by *Otsuka et al.* [2002] and *Camargo* [2009].

Once getting the slant TEC (STEC) in absolute value, we need to obtain a vertical TEC (VTEC) considering geometric relation between the satellite position, ionosphere, and ground receiver. The VTEC is obtained with STEC multiplied by a slant factor (S), which is defined as τ_0/τ_1, where τ_1 is the length of the ray path between altitudes of 250 and 450 km (assumed ionospheric slab) and τ_0 is the thickness of the ionosphere (assumed to be 200 km). The VTEC values are mapped on the ionospheric shell at a pierce point of the line of sight. The pierce points are obtained by assuming the ionospheric peak height to be 300 km altitude [*Otsuka et al.*, 2013]. The error in VTEC increases with increasing the zenith angle of the satellite-looking direction. This is mainly due to multipath error in the low elevation angle and the error in the instrument bias estimation. In the present method, satellites with the zenith angle less than 60°, i. e., the elevation angle more than 30° are used in calculation. The process of data handling and processing algorithm was based on that has been developed by *Otsuka et al.* [2002]. Table 1 lists the sequence of data processing from the RINEX original data to TEC data.

GNSS Ground-Based Receivers Over South America

There are four main GNSS receiver networks on the South American continent. Dual frequency GNSS receivers have been operated by IBGE (Brazilian Institute for Geography and Statistics). IBGE releases a package of RINEX format data (RBMC) from approximately 120 sites over Brazil, with 15 s time intervals [*Brazilian Institute for Geography and Statistics Website*, 2016]. RBMC real-time data are available through Networked Transport of RTCM via Internet Protocol. In addition to the RBMC data, the data from IGS (International GNSS Service) [*International GNSS Service Website*,

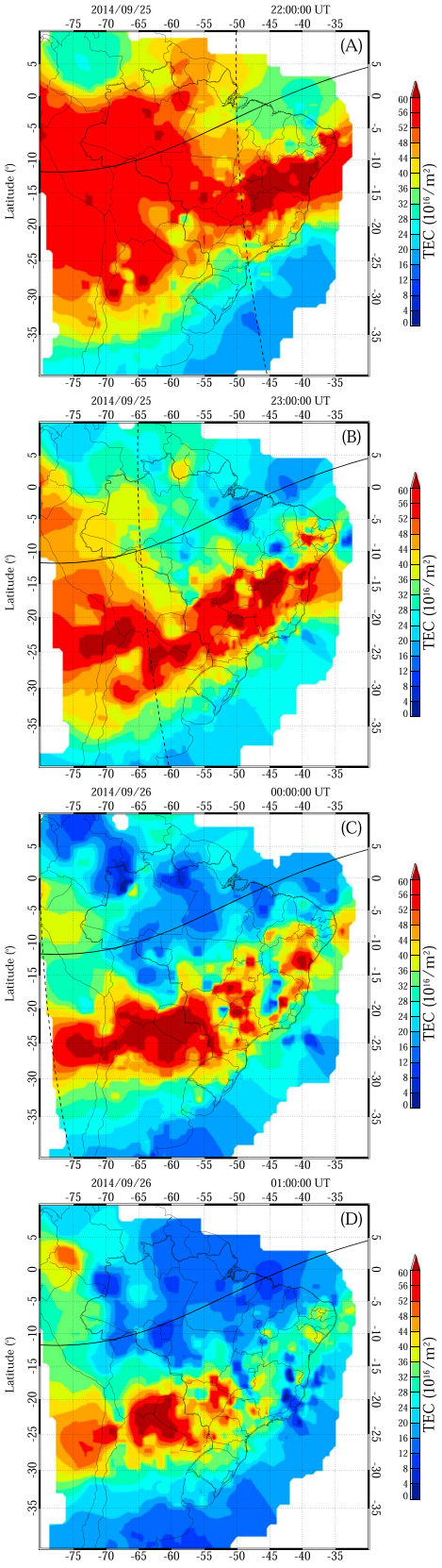

Figure 4. Same as Figure 3 but for 25–26 September 2014, showing development of the plasma depletions.

2016], LISN (Low-latitude Ionospheric Sensor Network) [*Low-latitude Ionospheric Sensor Network website*, 2016], and RAMSAC (Red Argentina de Monitoreo Satelital Continuo) [*Red Argentina de Monitoreo Satelital Continuo Website*, 2016] were also collected under collaboration scheme and processed at EMBRACE. Some additional information of these GNSS receiver networks has been reported elsewhere [*Takahashi et al.*, 2015].

Figure 1a demonstrates geographic locations of the GNSS receiver sites used in the present work. All of the area of Brazil, Peru, Chile, and Argentina are covered in this way. Only a few observation sites are available in the central part of South America (Bolivia and Paraguay). The total number of GNSS receivers over the entire continent is around 140. Normally, one receiver looks up simultaneously four to six GNSS satellites within the elevation angle larger than 30°. Therefore, a high density of TEC observation can be achieved. Figure 1b presents, as an example, ionospheric pierce points over South America at 01:20 UT, 19 February 2014. The total number of observation points is 646 in the present case. It can be seen that there is a relatively high-density observation area extending between 20°–30°S and 40°–60°W. Spatial resolution of 50 to 150 km can be achieved in this area. However, observation points were less in the low-latitude regions (0 to 15°S). In some areas, the distance larger than 500 km from one point to the other occurred, which makes it difficult to obtain the TEC spatial variations.

Spatial Resolution of TECMAP

TEC data were mapped on the ionospheric shell at 300 km altitude with a horizontal cell of 0.5° × 0.5° in latitude and longitude. In order to optimize the spatial resolution of TEC and to cover the entire area with TEC values, we first calculated a running average of the three cells; this corresponds to 3 × 3 elements covering an area of ~160 × 160 km^2. If no data were found in the area, the running average area expands to 5 × 5 elements, which corresponds to approximately 260 × 260 km^2. In this way, the running average element expands up to 21 × 21 elements, which corresponds to approximately 1000 × 1000 km^2 as an

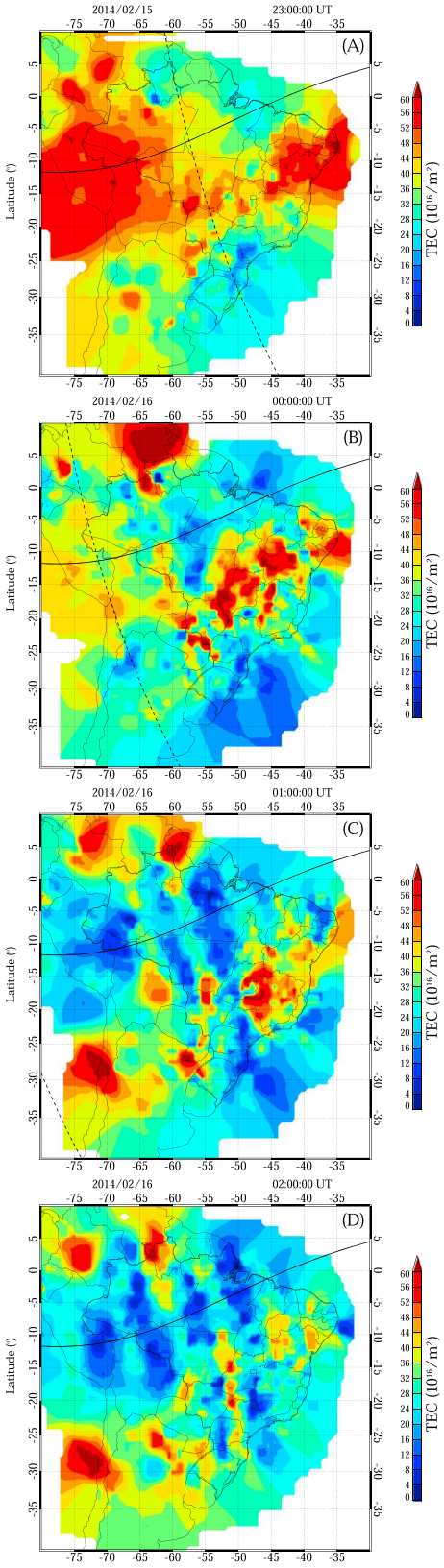

Figure 5. Same as Figure 3 but for 15–16 February 2014, from (a) 23:00 to (b) 00:00, (c) 01:00, and (d) 02:00 UT, showing an example of well-developed periodic plasma bubbles.

extreme case. The data processing method has been presented elsewhere [*Takahashi et al.*, 2015]. Figure 2 depicts distribution of binning from 3 × 3 (blue) to 11 × 11 (brown). Most of the southeastern area of Brazil and northern part of Argentina are covered by blue color boxes showing better spatial resolution than the other area. The spatial resolution of the TEC map, therefore, depends on the density of the observation sites. On average, the spatial resolution is approximately 50 to 100 km in the southeastern part of Brazil, 200–300 km in the northeastern part, and greater than 500 km in the Amazon region and the central part of the continent.

It should be noted that in the present mapping we assumed that the height of ionospheric shell is constant at 300 km altitude. However, the height is temporally variable. In the equatorial regions, it varies from the daytime (~250 km) to evening (>400 km). If we consider it, a pierce point displaces by more than 100 km from the assumed point depending on the satellite-viewing angle. Therefore, Figures 1b and 2 include a certain error in the ionospheric shell positioning.

Results

The present TECMAP can visualize the ionospheric total electron content (TEC) in a two-dimensional form. In the following subsections typical features of TECMAP with different physical conditions are presented.

Postsunset Equatorial Ionization Anomaly

Figures 3a–3d present TEC distribution over South America during the early evening on 31 August 2014. Daytime EIA is ceasing at 21:00 UT (Figure 3a). During the 22:00–23:00 UT period (Figures 3b and 3c) the plasma density at the eastern coast (30–40°W) started to decrease. The postsunset ionization anomaly (PS-EIA) was developed to form the equatorial plasma trough along the geomagnetic equator (a curved full line in the figure) and to

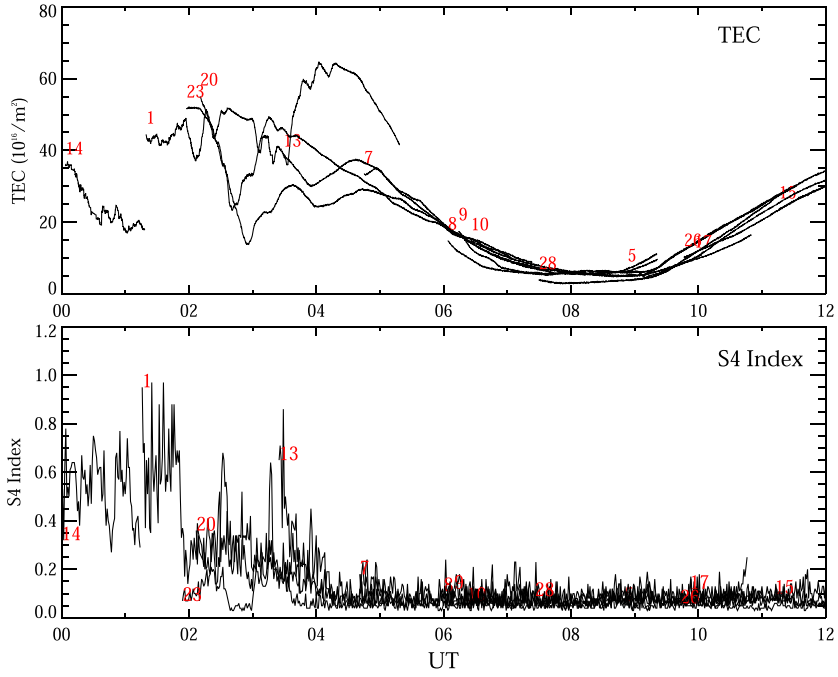

Figure 6. (top) Vertical TEC and (bottom) the amplitude scintillation index S4 observed at Dourados (22.2 S, 50.0 W) on 16 February 2014. The number corresponds to PRN.

generate plasma crests over the off-equatorial region, both in the Northern and Southern Hemispheres. The solar terminator at 300 km altitude (a dashed line) indicates the condition of astronomical twilight when the ionization process ceased. At 00:00 UT (Figure 3d) the PS-EIA is well developed. Some irregular distribution of TEC can be seen in the southern crest belt.

Plasma Bubble Formation and Development

During the September equinox, the daytime EIA is well developed at 21:00 UT as shown in Figure 4a. At 23:00 UT (Figure 4c), the PS-EIA was developed and a deep plasma trough along the magnetic equator can be seen. Inside of the trough there seems to be plasma density variations along the longitudinal zone, and those are perpendicular to the magnetic equator. The plasma density depletions are very clear in the map of 00:00 UT (Figure 4d), showing a signature of plasma bubbles at around (15°S, 50°W). It can be seen that the plasma bubbles are penetrating into the crest belt cutting it in several pieces. The distance between the bubbles seems to be around 700 km in longitude.

The plasma bubble activity becomes more intense from October to November, and it continues up to March. The bubbles are frequently formed with a periodic distance structure along the longitudinal direction. Figures 5a–5d show well-developed periodic plasma bubbles observed on the night of 15–16 February 2014. While the solar terminator advanced westward, periodic depletions occurred in the magnetic equator region (Figures 5b and 5c). At 02:00 UT (Figure 5d) there are four to five bubbles in development and drifting eastward. Some of them are extended up to 30°S. The longitudinal distance between the bubbles is around 600 km. The amplitude of TEC depletion (from the peak to bottom) reaches around 40–50 TECU. It means that the horizontal gradient of TEC from the peak to bottom of the bubble is ~15 TECU/100 km. Such a large scale and large amplitude of the plasma density variation in space and time make it difficult to predict ionospheric error range in the satellite-based positioning system.

Plasma bubbles also cause radio wave scintillations. Deterioration of the GPS radio waves by scintillation is another concern in operation of the positioning system. Figure 6 depicts temporal variation of the TEC and GPS signal amplitude scintillation index "S4" observed at Dourados (22.2°S, 54.9°W) on 16 February 2015. Each line with numbering (PRN) corresponds to the observation of individual GPS satellite. Only those PRNs with the elevation angle larger than 30° were selected. As shown in Figure 5 several plasma bubbles passed over the site during the night. The large TEC variations observed from 00:00 to

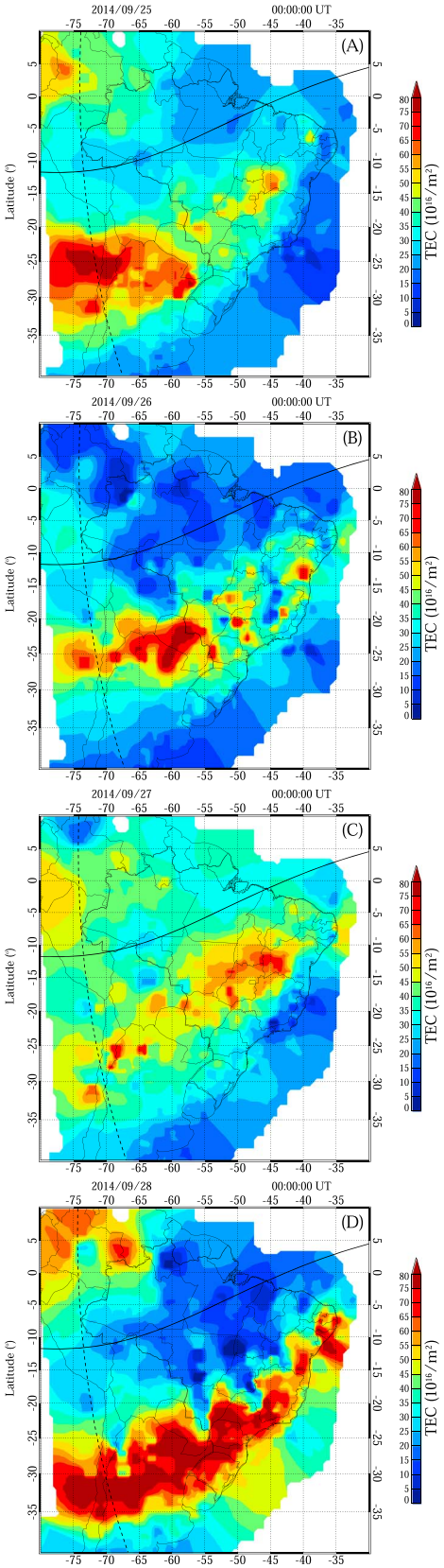

Figure 7. Day-to-day variability of TECMAP over South America from (a–d) 25 to 28 September 2014, at a fixed time 00:00 UT (21:00 LT at 45°W).

05:00 UT in Figure 6 are, therefore, due to the passage of plasma bubbles. It should be remembered that each PRN demonstrates temporal variation at different ionospheric pierce points. Large difference of TEC values between the PRNs should cause a large ionospheric error range for single-frequency positioning system.

The S4 is an index of amplitude variation of GPS radio waves. It is obtained from a ratio of standard deviation of the received signal intensity (measured by a 50 Hz sampling rate) to the averaged during 1 min time interval including noise of the receiver. The value of ~0.1 is a noise level. S4 has a range of 0 to 1.0 from no disturbance to the most intense level of scintillation, respectively. It is considered that the signal is strongly affected if S4 is larger than 0.2 [*Moraes et al.*, 2013]. In the present case S4 varied between 0.1 and 0.9 from 00:00 to 04:00 UT which corresponds to the period of plasma bubble passage. Each PRN showed different amplitudes of oscillation. During the period, therefore, the GPS positioning system would be affected and needs a special attention in the data analysis.

Day-To-Day Variability of the Plasma Bubble Activity

Figures 7a–7d show TECMAP over South America from 25 to 28 September 2014, four consecutive nights at 00:00 UT (nighttime over the continent). In the night of 24–25 September (Figure 7a), PS-EIA was developed but showing longitudinal gradient of the TEC intensity. The anomaly trough was, however, not developed (20–30 TECU), and the plasma bubble activity was weak. In the next night (26 September), Figure 7b, the equatorial trough was deep (less than 20 TECU) and plasma bubbles were developed extending up to 20–25°S. On the other hand, PS-EIA was not developed in the night of 27 September (Figure 7c) and the crest was located at around 12°S at 45°W. No clear generation of plasma bubbles was observed. On 28 September (Figure 7d), again, the PS-EIA became strong (TEC > 75) and well-developed plasma bubbles could be

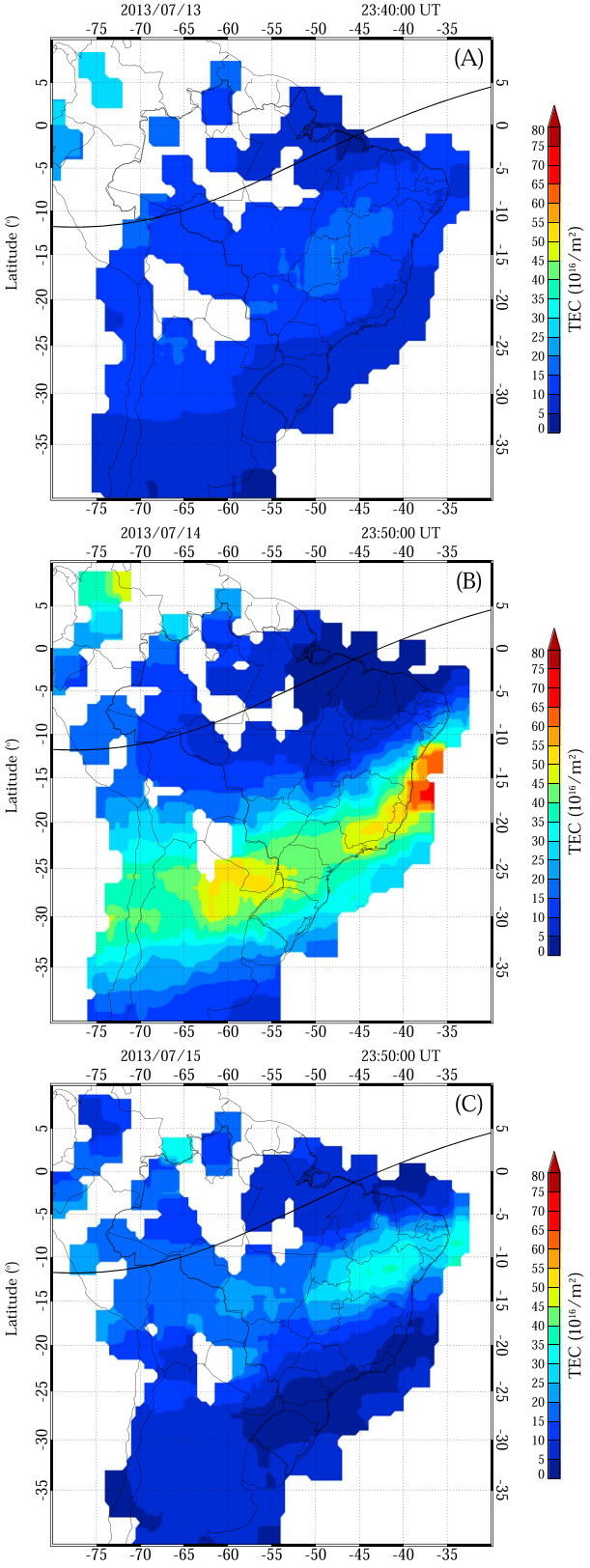

Figure 8. TECMAP of (a) 13 July, (b) 14, and (c) 15, in 2013, at a fixed time 23:50 UT during the geomagnetic storm period.

seen. There was no geomagnetic activity during the period (*Kp* was less than 4). The plasma bubble activity is high over South America during the summer months (September to March). However, the day-to-day variability of the activity was not well known [*Sobral et al.*, 2002]. The large day-to-day variability of the bubble occurrence observed in the present work makes it difficult to predict bubble activities; when and where does it occur?

Geomagnetic Storm Event

Figures 8a–8c show TECMAPs of three consecutive evenings of before (13 July 2013), during (14 July), and after (15 July) the geomagnetic storm event. For reference temporal variation of the magnetometer *H* component at Eusebio (3.8°S, 38.4°W), *Dst* and *AE* indices during the storm are shown in Figures 9a–9c. The main phase of the storm occurred at around 21:00 to 23:30 UT on the night of 14 July 2013. The planetary *K* index (*Kp*) was 4 to 5, *Dst* was around −75 nT, and the *AE* index varied from 700 to 1200 nT. Although the storm was somewhat moderate, the influence of the storm for the equatorial ionosphere looks to be significant, particularly for the EIA formation. During the main phase (14 July) the TECMAP (Figure 8b) demonstrates strong development of the PS-EIA forming the anomaly crest far from the geomagnetic equator. On the other hand, TECMAPs of the day before (Figure 8a) and the day after (Figure 8c) showed a weak formation of PS-EIA. Normally, EIA is weak during the June–July season in the Southern Hemisphere.

It should be noted that the main phase occurred during the evening time over the South America. Ionosonde at São Luis (2.6°S, 44.2°W) showed strong uplifting of *F* layer. The *F* layer bottom height was above 800 km altitude around 23:30 UT on 14 July. It was around 400–500 km altitudes in the previous night and the day after. The uplifting of the *F* layer during the storm

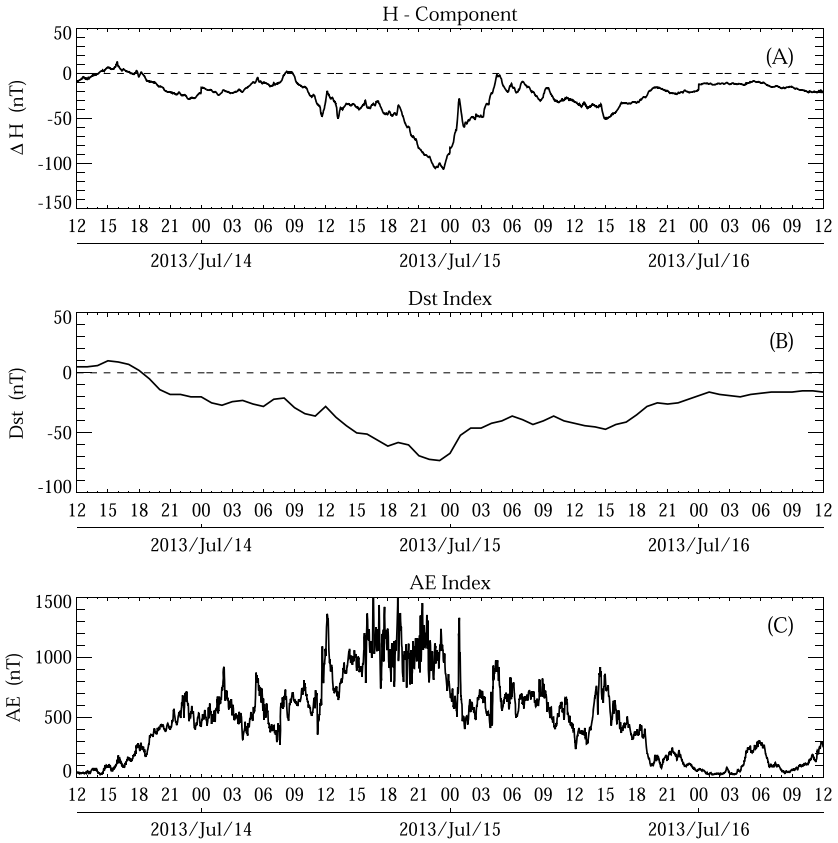

Figure 9. (a) Magnetometer *H* component at Euzebio (38.4°W, 3.8°S), (b) *Dst* index, and (c) *AE* index during the period of 13–16 July 2013. The storm main phase occurred at around 23:00 UT on 14 July 2013.

time happens because of the additional **E × B** effect caused by the prompt penetration electric field from the auroral region [*Abdu et al*., 2003]. It is interesting to note that the *AE* index suddenly decreased from 1000 nT to 500 nT at 23:00 UT when the magnetometer *H* component and *Dst* index entered in a recovering phase. The *F* layer uplifting also ceased. The observed day-to-day variation of the PS-EIA (Figures 8a–8c) can be explained by the variation of *F* layer uplifting. The response of the equatorial ionosphere against geomagnetic storms is variable. It depends on the strength of the solar wind, the vertical component of the interplanetary magnetic field (B_z), auroral activity (*AE*), and also observer's local time (dayside, evening, or nightside). The development of EIA is affected by such high-latitude auroral activities. The present TEC mapping could monitor it in a global scale.

Discussion

As presented in the previous section, TECMAP is a useful tool to monitor the ionosphere. Equatorial and low-latitude ionosphere is very active and dynamic. Temporal and spatial variations of the equatorial ionization anomaly (plasma trough and crest) and plasma irregularities (depletions/bubbles) are very rapid and steep. TEC mapping with a 10 min time sequence is necessary to monitor such rapid variations. In the present work, however, the spatial resolution is not sufficient to depict fine details of the EIA crest and plasma bubbles. Plasma bubbles frequently demonstrate fine structures of 10 to 100 km [*Takahashi et al*., 2009]. Our present mapping process (moving average technique) is dependent on the density of observation point (ionospheric pierce points). The expected spatial resolution is around 50 to 100 km in the best case as mentioned before.

Figure 10 demonstrates mosaic of TEC mapping over the southeastern coast of Brazil between the latitude of 15° to 30°S. The smallest square in the map is ~45 km of width in this latitudinal zone. A couple of north-south aligned TEC depletions with 50 to 100 km longitudinal width can be seen; those are signatures of the plasma bubbles. However, it is not the case in the equatorial and low-latitude region of Brazil (0° to 15°S) where the

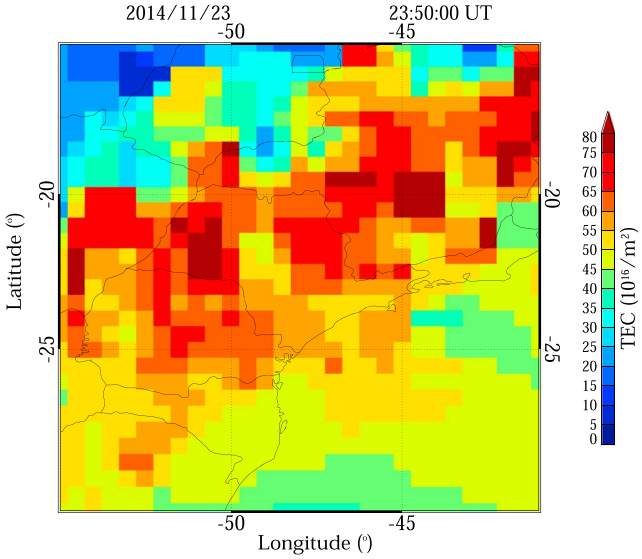

Figure 10. Expanded TEC map over the southeast region of Brazil taken at 23:50 UT on 23 November 2014. One mosaic box corresponds to ~45 × 45 km width.

number of observation points is less. The spatial resolution becomes large with 300 to 500 km. In order to improve the spatial resolution in the northern part of Brazil, further dense ground-based GNSS receiver network is necessary. It should be pointed out in Figure 10 that the plasma bubble causes a strong horizontal gradient of TEC. It reaches more than 50 TECU in a distance of 100 km, and it corresponds to an ionospheric range error of ~8 m.

Figure 11 shows an example of vertical ionospheric range error on 16 February 2014, at 01:00 UT. It was obtained from the relation of TEC and the range delay presented in the previous section (equation (2)). The color shade map is similar to that obtained in Figure 5c, except spatially interpolated contour lines indicating the error range from 1 to 6 m. It should be noted that Figure 11 does not inform positioning error of the observer but a spatially averaged vertical range delay. Such results, if made available with appropriated file format like IONEX (IONosphere map EXchange) for example, can be used to apply corrections to the single-frequency measurement with quality better than the broadcasted ones, like the Klobuchar model [*Klobuchar*, 1987]. IONEX files can be produced initially in postprocessing mode and in the future in near real time. Real-time monitoring (nowcasting) of the ionosphere together with its associated errors is, therefore, an important issue.

In order to improve the spatial resolution of TECMAP, further dense network of ground-based GNSS receivers would be necessary. In addition to the ground-based efforts, inclusion of satellite-based observation of TEC would also be important. Constellation Observing System for Meteorology, Ionosphere, and Climate satellite mission [*Constellation Observing System for Meteorology, Ionosphere, and Climate website*, 2016] has been producing a global TEC data since 2006. Inclusion of satellite-based data would make the present TECMAP much useful for GNSS-based positioning system users.

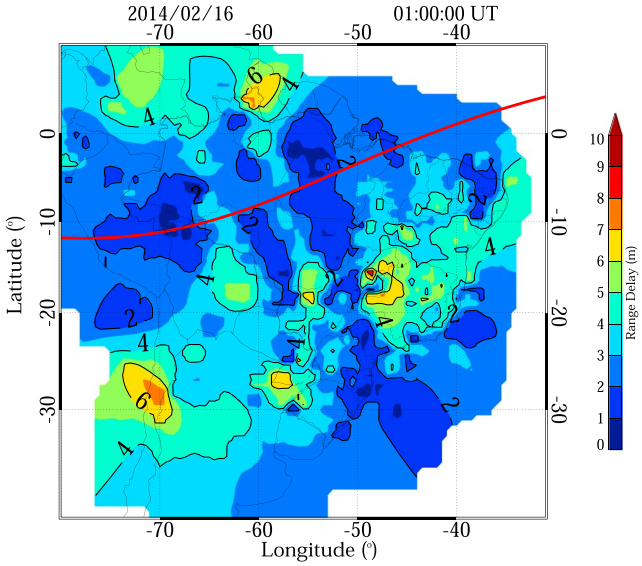

Figure 11. Estimated vertical range error over South America on 16 February 2014, at 01:00 UT. The numbers in the contour map indicate the error range in meters.

Summary

Ionospheric TEC maps over South America were produced with the purpose of space weather application. Spatial resolution of the map varied from 50 to 100 km in the southeastern region of Brazil, 200–300 km in the northeastern area and greater than 500 km in the Amazon region. TECMAPs are produced in every 10 min with a time delay of 12 h. Near real-time TECMAP is also available using real-time data handling from the limited (~40) RBMC/IBGE sites. Development of the equatorial ionization anomaly (EIA), postsunset anomaly

(PS-EIA), and plasma bubble activities could be successfully monitored. Frequently TEC spatial gradient reached the amplitude of around 50 TECU in a horizontal distance of less than 100 km, which corresponds to approximately 8 m of the vertical range delay. Monitoring of the spatial and temporal variations of TEC and GNSS signal scintillation is an important issue not only for academic research but also for social infrastructure concern. The present TECMAP will be useful to apply in the data assimilation ionospheric model for GNSS-based positioning system.

Acknowledgments
The data used in the present work are available at EMBRACE website [*EMBRACE site*, 2016]. The GNSS ground-based receiver data were collected from different GNSS networks in South America: RBMC of IBGE, RAMSAC of Argentina, and IGS and LISN of Boston University. We are grateful to these network sites for providing the data continuously. Without their data, it would not be possible to produce such TECMAP. The present work was partially supported by CNPq under the grant 30.5461/2015-0. C.M. Denardini thanks CNPq/MCTI (grant 303121/2014-9) and FAPESP (grant 2012/08445-9). E.R. de Paula is grateful to CNPq (grant 310802/2015-6). K. Shiokawa and Y. Otsuka also thank the support by JSPS KAKENHI (grant 15H05815).

References

Abdu, M. A., I. S. Batista, H. Takahashi, J. MacDougall, J. H. Sobral, A. F. Medeiros, and N. B. Trivedi (2003), Magnetospheric disturbance induced equatorial plasma bubble development and dynamics: A case study in Brazilian sector, *J. Geophys. Res.*, *108*(A12), 1449, doi:10.1029/2002JA009721.

Bagiya, M. S., H. P. Joshi, K. N. Iyer, M. Aggarwal, S. Ravindran, and B. M. Pathan (2009), TEC variations during low solar activity period (2005–2007) near the Equatorial Ionospheric Anomaly Crest region in India, *Ann. Geophys.*, *27*, 1047–1057.

Belwitt, G. (1990), An automatic editing algorithm for GPS data, *Geophys. Res. Lett.*, *17*, 199–202, doi:10.1029/GL017i003p00199.

Camargo, P. O. (2009), Quality of TEC estimated with Mod Ion using GPS and GLONASS data, *Math. Probl. Eng.*, *2009*, 794578, doi:10.1155/2009/794578.

Constellation Observing System for Meteorology, Ionosphere, and Climate website (2016). [Available at http://www.cosmic.ucar.edu/index.html.]

Estudo e Monitoramento Brasileiro de Clima Especial (EMBRACE) site (2016). [Available at http://www2.inpe.br/climaespacial/portal/en/.]

Federal Aviation Administration (2016), Satellite Navigation Ground Based Augmentation System (GBAS), Fed. Aviat. Admin. [Available at http://laas.tc.faa.gov/.]

Hoffmann-Wellenhof, B., H. Lichtenegger, and J. Collins (1994), *GPS Theory and Practice*, 3rd rev. ed., Springer, Vienna.

Brazilian Institute for Geography and Statistics Website (2016). [Available at http://www.ibge.gov.br/home/geociencias/geodesia/rbmc/rbmc_est.shtm.]

International GNSS Service Website (2016). [Available at http://www.igs.org.]

Kantor, I. J., M. Fedrizzi, and E. R. de Paula (2000), Total ionospheric electron content from GPS measurements over the Brazilian region, *Geofis. Int.*, *39*(1), 81–85.

Kelley, M. C. (2009), *The Earth's Ionosphere: Plasma Physics and Electrodynamics*, *Int. Geophys. Ser.*, vol. 96, Academic Press, San Diego, Calif.

Kintner, P. M., B. M. Ledvina, and E. R. de Paula (2007), GPS and ionospheric scintillations, *Space Weather*, *5*, S09003, doi:10.1029/2006SW000260.

Klobuchar, J. A. (1987), Ionospheric time-delay algorithm for single-frequency GPS users, *IEEE Trans. Aerosp. Electron. Syst.*, *23*(3), 325–331.

Low-latitude Ionospheric Sensor Network website (2016). [Available at http://lisn.igp.gob.pe.]

Moraes, A. O., E. R. de Paula, W. J. Perrella, and F. S. Rodrigues (2013), On the distribution of GPS signal amplitudes during low-latitude ionospheric scintillation, *GPS Solutions*, doi:10.1007/s10291-012-0295-3.

Nogueira, P. A. B., et al. (2015), Modeling the equatorial and low-latitude ionospheric response to an intense X-class solar flare, *J. Geophys. Res. Space Physics*, *120*, 3021–3032, doi:10.1002/2014JA020823.

International Association of Oil & Gas Producers (2011), Guidelines for GNSS positioning in the oil & gas industry, *Rep. 373-19*, Int. Assoc. of Oil & Gas Prod. (OGP), IMCA & OGP, June. [Available at http://www.ogp.org.uk/pubs/373-19.pdf.]

Otsuka, Y., T. Ogawa, A. Saito, T. Tsugawa, S. Fukao, and S. Miyazaki (2002), A new technique for mapping of total electron content using GPS network in Japan, *Earth Planets Space*, *54*, 63–70.

Otsuka, Y., K. Suzuki, S. Nakagawa, M. Nishioka, K. Shiokawa, and T. Tsugawa (2013), GPS observations of medium-scale traveling ionospheric disturbances over Europe, *Ann. Geophys.*, *31*, 163–172, doi:10.5194/angeo-31-163-2013.

Red Argentina de Monitoreo Satelital Continuo Website (2016). [Available at http://www.ign.gob.ar/NuestrasActividades/Geodesia/Ramsac.]

Schrijver, C. J., et al. (2015), Understanding space weather to shield society: A global road map for 2015–2025 commissioned by COSPAR and ILWS, *Adv. Space Res.*, *55*(12), 2745–2807, doi:10.1016/j.asr.2015.03.023.

Sobral, J. H. A., M. A. Abdu, H. Takahashi, M. J. Taylor, E. R. de Paula, C. J. Zamlutti, and G. L. Borba (2002), A study of the ionospheric plasma bubbles climatology over Brazil based on 22 years (1977–1998) of OI 630 nm airglow observation, *J. Atmos. Terr. Phys.*, *64*(12–14), 1517–1524.

Stafford, J. V. (2000), Implementing precision agriculture in the 21st century, *J. Agric. Eng. Res.*, *76*, 267–275, doi:10.1006/jaer.2000.0577.

Takahashi, H., et al. (2009), Simultaneous observation of ionospheric plasma bubbles and mesospheric gravity waves during the SpreadFEx Campaign, *Ann. Geophys.*, *27*, 1477–1487.

Takahashi, H., C. M. Wrasse, Y. Otsuka, A. Ivo, V. Gomes, I. Paulino, A. F. Medeiros, C. M. Denardini, N. Sant'Anna, and K. Shiokawa (2015), Plasma bubble monitoring by TECmap and 630 nm airglow image, *J. Atmos. Sol. Terr. Phys.*, *130–131*, 151–158, doi:10.1016/j.jastp.2015.06.003.

Dr. H. Takahashi *is a professor at Instituto Nacional de Pesquisas Espaciais in São José dos Campos, Brazil. E-mail:hisao.takahashi@inpe.br.*

Dr. C. M. Wrasse *is a researcher at Instituto Nacional de Pesquisas Espaciais in São José dos Campos, Brazil.*

Dr. C. M. Denardini *is a researcher at Instituto Nacional de Pesquisas Espaciais in São José dos Campos, Brazil.*

Dr. M. B. Pádua *is a researcher at Instituto Nacional de Pesquisas Espaciais in São José dos Campos, Brazil.*

Dr. E. R. de Paula *is a professor at Instituto Nacional de Pesquisas Espaciais in São José dos Campos, Brazil.*

Dr. S. M. A. Costa *is a researcher at Instituto Brasileiro de Geografia e Estatística – IBGE in Rio de Janeiro, Brazil.*

Dr. Y. Otsuka *is an Associate Professor at Institute for Space-Earth Environmental Research (ISEE), Nagoya University in Nagoya, Japan.*

Dr. K. Shiokawa *is a professor at Institute for Space-Earth Environmental Research (ISEE), Nagoya University in Nagoya, Japan.*

Dr. J. F. Galera Monico *is a professor at Universidade Estadual Paulista in Presidente Prudente, Brazil.*

Ms. A. Ivo *is a researcher at Instituto Nacional de Pesquisas Espaciais in São José dos Campos, Brazil.*

Dr. N. Sant'Anna *is a professor at Instituto Nacional de Pesquisas Espaciais in São José dos Campos, Brazil.*